

# Gravitational wave sensitivity curves

C J Moore<sup>1</sup>, R H Cole<sup>1</sup> & C P L Berry<sup>1,2</sup>

<sup>1</sup> Institute of Astronomy, Madingley Road, Cambridge, CB3 0HA, United Kingdom

<sup>2</sup> School of Physics and Astronomy, University of Birmingham, Edgbaston, Birmingham B15 2TT, United Kingdom

E-mail: [cjm96@ast.cam.ac.uk](mailto:cjm96@ast.cam.ac.uk)

**Abstract.** There are several common conventions in use by the gravitational wave community to describe the amplitude of sources and the sensitivity of detectors. These are frequently confused. We outline the merits of and differences between the various quantities used for parameterizing noise curves and characterizing gravitational wave amplitudes. We conclude by producing plots that consistently compare different detectors. Similar figures can be generated on-line for general use at <http://www.ast.cam.ac.uk/~rhc26/sources/>.

PACS numbers: 04.30.-w, 04.30.Db, 04.80.Nn, 95.55.Ym

## 1. Introduction

The next few years promise to deliver the first direct detection of gravitational waves (GWs). This will most likely be achieved by the advanced Laser Interferometer Gravitational-wave Observatory (LIGO; Harry, 2010) and advanced Virgo (Acernese et al., 2009) detectors operating in the frequency range (10–10<sup>3</sup>) Hz. By the end of the decade, it is expected that pulsar timing arrays (PTAs; Foster and Backer, 1990) will also detect very low frequency GWs around 10<sup>−8</sup> Hz. Further into the future, space-based detectors, such as the evolved Laser Interferometer Space Antenna (eLISA; Seoane et al., 2013), will probe GWs in the millihertz regime. These advances shall herald the beginning of multi-wavelength GW astronomy as a means of observing the Universe.

There already exists an extensive literature assessing the potential of all of these detectors to probe the astrophysics of various sources. There are several different methods commonly used to describe the sensitivity of a GW detector and the strength of a GW source. It is common practice to summarise this information on a sensitivity-curve plot. When producing these plots, it is desirable to have a consistent convention between detectors and sources that allows information about both to be plotted on the same graph. Ideally, the detectors and sources are represented in such a way that the relative detectability of the signals is immediately apparent.

In this work, we discuss the differing conventions commonly used in GW astronomy. The amplitude of a GW is a strain, a dimensionless quantity  $h$ . This gives a fractional change in length, or equivalently light travel time, across a detector. The strain is small, making it a challenge to measure: we are yet to obtain a direct detection of a GW. To calibrate our expectations for future detections it is necessary to quantify the sensitivity of our instruments and the strength of their target signals. When discussing the loudness of sources and the sensitivity of detectors there are three commonly used parametrizations based upon the strain: the characteristic strain, the power spectral density (PSD) and the spectral energy density. We aim to disambiguate these three and give a concrete comparison of different detectors. It is hoped that this will provide a useful reference for new and experienced researchers in this field alike.

We begin by expounding the various conventions and the relationships between the conventions in sections 2 and 3. A review of GW detectors (both current and proposed) is given in section 4 and a review of GW sources is given in section 5. In Appendix A several example sensitivity curves are presented. A website where similar figures can be generated is available at [www.ast.cam.ac.uk/~rhc26/sources/](http://www.ast.cam.ac.uk/~rhc26/sources/). Here, the user may select which sources and detectors to include to tailor the figure to their specific requirements.

## 2. Signal parametrization

### 2.1. Signal analysis preliminaries

Gravitational radiation has two independent polarization states denoted  $+$  and  $\times$ ; a general signal can be described as a linear combination of the two polarization states,  $h = A_+ h_+ + A_\times h_\times$ . The sensitivity of a detector to these depends upon the relative orientations of the source and detector. The output of a gravitational wave detector  $s(t)$  contains a superposition of noise  $n(t)$  and (possibly) a signal  $h(t)$ ,

$$s(t) = n(t) + h(t) . \quad (1)$$

We shall have recourse to work with the Fourier transform of the signal, using the conventions that

$$\tilde{x}(f) = \mathcal{F}\{x(t)\}(f) = \int_{-\infty}^{\infty} dt x(t) \exp(-2\pi i f t) , \quad (2)$$

$$x(t) = \mathcal{F}^{-1}\{\tilde{x}(f)\}(t) = \int_{-\infty}^{\infty} df \tilde{x}(f) \exp(2\pi i f t) . \quad (3)$$

For simplicity, it is assumed that the noise in the GW detector is stationary and Gaussian (with zero mean); under these assumptions the noise is fully characterised via the one-sided noise PSD  $S_n(f)$ ,

$$\langle \tilde{n}(f) \tilde{n}^*(f') \rangle = \frac{1}{2} \delta(f - f') S_n(f) , \quad (4)$$

where angle brackets  $\langle \dots \rangle$  denote an ensemble average over many noise realisations (Cutler and Flanagan, 1994). In reality, we have only a single realisation to work with, but the ensemble average can be replaced by a time average for stationary stochastic noise. The procedure is to measure the noise over a sufficiently long duration  $T$  and then compute the Fourier transform  $\tilde{n}(f)$  with a frequency resolution  $\Delta f = T^{-1}$ ; this is repeated many times to give an average. The noise PSD  $S_n(f)$  has units of inverse frequency.

Since the GW signal and detector output are both real it follows that  $\tilde{h}(-f) = \tilde{h}^*(f)$  and  $\tilde{n}(-f) = \tilde{n}^*(f)$ ; therefore,  $S_n(f) = S_n(-f)$ . The fact that  $S_n(f)$  is an even function means that Fourier integrals over all frequencies can instead be written as integrals over positive frequencies only, e.g., (8) and (14); it is for this reason that  $S_n(f)$  is called the *one-sided* PSD.<sup>‡</sup>

When integrated over all positive frequencies, the PSD gives the mean square noise amplitude. Starting by taking the time average of the square of the detector noise:

$$\overline{|n(t)|^2} = \lim_{T \rightarrow \infty} \frac{1}{2T} \int_{-T}^T dt \, n(t) n^*(t) \quad (5)$$

$$\begin{aligned} &= \lim_{T \rightarrow \infty} \frac{1}{2T} \int_{-T}^T dt \int_{-\infty}^{\infty} df \int_{-\infty}^{\infty} df' \tilde{n}(f) \tilde{n}^*(f') \exp(2\pi i f t) \exp(-2\pi i f' t) \\ &= \lim_{T \rightarrow \infty} \frac{1}{2T} \int_{-T}^T dt \int_{-\infty}^{\infty} df \int_{-\infty}^{\infty} df' \mathcal{F}\{n(\tau)\}(f) [\mathcal{F}\{n(\tau)\}(f')]^* \\ &\quad \times \exp(2\pi i f t) \exp(-2\pi i f' t) , \end{aligned} \quad (6)$$

where we have substituted in using the definitions of the Fourier transform and its inverse. A property of Fourier transforms is that a time-domain translation by amount  $t$  is equivalent to a frequency-domain phase change  $2\pi f t$ ; if  $\mathcal{F}\{n(\tau)\}(f) = \tilde{n}(f)$ , then  $\mathcal{F}\{n(\tau - t)\}(f) = \tilde{n}(f) \exp(2\pi i f t)$ . Therefore, the exponential factors in (6) may be absorbed as

$$\overline{|n(t)|^2} = \lim_{T \rightarrow \infty} \frac{1}{2T} \int_{-T}^T dt \int_{-\infty}^{\infty} df \int_{-\infty}^{\infty} df' \mathcal{F}\{n(\tau - t)\}(f) [\mathcal{F}\{n(\tau - t)\}(f')]^* . \quad (7)$$

Since the noise is a randomly varying signal, we can use the ergodic principle to equate a time average, denoted by  $\overline{(\dots)}$ , with an ensemble average, denoted by  $\langle \dots \rangle$ . The noise is stationary, consequently, its expectation value is unchanged by the time-translation performed above. Therefore, using (4), the mean square noise amplitude is given by

$$\overline{|n(t)|^2} = \int_{-\infty}^{\infty} df \int_{-\infty}^{\infty} df' \langle \tilde{n}(f) \tilde{n}^*(f') \rangle \quad (8)$$

$$\begin{aligned} &= \int_{-\infty}^{\infty} df \int_{-\infty}^{\infty} df' \frac{1}{2} S_n(f) \delta(f - f') \\ &= \int_0^{\infty} df \, S_n(f) . \end{aligned} \quad (9)$$

<sup>‡</sup> An alternative convention is to use the two-sided PSD  $S_n^{(2)}(f) = S_n(f)/2$ .

Given a detector output, the challenge is to extract the signal. There is a well known solution to this problem that involves constructing a Wiener optimal filter (Wiener, 1949). Let  $K(t)$  be a real filter function with Fourier transform  $\tilde{K}(f)$ . Convoluting this with the detector output gives a contribution from the signal and a contribution from the noise,

$$(s * K)(\tau) = \int_{-\infty}^{\infty} dt [h(t) + n(t)] K(t - \tau) \approx \mathcal{S} + \mathcal{N}. \quad (10)$$

The signal contribution  $\mathcal{S}$  is defined as the expectation of the convolution in (10) when a signal is present, maximised by varying the offset to achieve the best overlap with the data. Since the expectation of pure noise is zero it follows that

$$\mathcal{S} = \int_{-\infty}^{\infty} dt h(t) K(t) = \int_{-\infty}^{\infty} dt h(t) K^*(t) = \int_{-\infty}^{\infty} df \tilde{h}(f) \tilde{K}^*(f). \quad (11)$$

The squared contribution from noise  $\mathcal{N}^2$  is defined as the mean square of the convolution in (10) when no signal is present,

$$\begin{aligned} \mathcal{N}^2 &= \int_{-\infty}^{\infty} dt \int_{-\infty}^{\infty} dt' K(t) K(t') \langle n(t) n(t') \rangle \\ &= \int_{-\infty}^{\infty} dt \int_{-\infty}^{\infty} dt' K(t) K^*(t') \int_{-\infty}^{\infty} df \int_{-\infty}^{\infty} df' \langle \tilde{n}(f) \tilde{n}^*(f') \rangle \exp[2\pi i(ft - f't')] \\ &= \int_{-\infty}^{\infty} df \frac{1}{2} S_n(f) \tilde{K}(f) \tilde{K}^*(f), \end{aligned} \quad (12)$$

using the definition of  $S_n(f)$  from (4). Hence the signal-to-noise ratio (SNR)  $\varrho$  is given by

$$\varrho^2 = \frac{\mathcal{S}^2}{\mathcal{N}^2} = \frac{\left( \frac{1}{2} S_n(f) \tilde{K}(f) \middle| \tilde{h}(f) \right)^2}{\left( \frac{1}{2} S_n(f) \tilde{K}(f) \middle| \frac{1}{2} S_n(f) \tilde{K}(f) \right)}, \quad (13)$$

where we have introduced the inner product between signal  $\tilde{A}$  and  $\tilde{B}$  as (Finn, 1992)

$$\left( \tilde{A}(f) \middle| \tilde{B}(f) \right) = 4\Re \left\{ \int_0^{\infty} df \frac{\tilde{A}^*(f) \tilde{B}(f)}{S_n(f)} \right\}. \quad (14)$$

The optimum filter is that function  $\tilde{K}(f)$  which maximises the SNR in (13). From the Cauchy–Schwarz inequality, it follows that the optimum filter is

$$\tilde{K}(f) = \frac{\tilde{h}(f)}{S_n(f)}. \quad (15)$$

This is the Wiener filter, which may be multiplied by an arbitrary constant since this does not change the SNR. Using this form for  $\tilde{K}(f)$ , the squared SNR is

$$\varrho^2 = \int_0^{\infty} df \frac{4|\tilde{h}(f)|^2}{S_n(f)} = \left( \tilde{h}(f) \middle| \tilde{h}(f) \right). \quad (16)$$

In order to construct the Wiener filter, it is necessary to know *a priori* the form of the signal,  $\tilde{h}(f)$ , for this reason the Wiener filter is sometimes called the *matched* filter.

Whilst the magnitude of the Fourier transform of the signal  $|\tilde{h}(f)|$  provides a simple quantification of the GW amplitude as a function of frequency, it has one main deficiency. For an inspiralling source, the instantaneous amplitude can be orders of magnitude below the noise level in a detector; however, as the signal continues over many orbits, the SNR can be integrated up to a detectable level. It is useful to have a quantification of the GW amplitude that accounts for this effect; three such methods are described in the following subsections.

## 2.2. Characteristic strain

The characteristic strain  $h_c$  is designed to include the effect of integrating an inspiralling signal. Its counterpart for describing noise is the noise amplitude  $h_n$ . These are defined as

$$[h_c(f)]^2 = 4f^2 \left| \tilde{h}(f) \right|^2, \quad (17)$$

$$[h_n(f)]^2 = f S_n(f), \quad (18)$$

such that the SNR in (16) may be written

$$\varrho^2 = \int_{-\infty}^{\infty} d(\log f) \left[ \frac{h_c(f)}{h_n(f)} \right]^2. \quad (19)$$

The strain amplitudes  $h_c(f)$  and  $h_n(f)$  are dimensionless. Using this convention, when plotting on a log–log scale, the area between the source and detector curves is related to the SNR via (19). This convention allows the reader to integrate by eye to assess the detectability of a given source (see figure A1).

An additional advantage of this convention is that the values on the strain axis for the detector curve  $h_n(f)$  have a simple physical interpretation: they correspond to the root-mean-square noise in a bandwidth  $f$ . One downside to plotting characteristic strain is that the values on the strain axis  $h_c(f)$  do not directly relate to the amplitude of the waves from the source. Another disadvantage is that the characteristic strain for a monochromatic source is infinite.

## 2.3. Power spectral density

A second commonly used quantity for sensitivity curves is the square root of the PSD or the amplitude spectral density (see figure A2). When discussing a detector, rearranging (18) gives

$$\sqrt{S_n(f)} = h_n(f) f^{-1/2}; \quad (20)$$

by analogy, we can define an equivalent for source amplitudes

$$\sqrt{S_h(f)} = h_c(f) f^{-1/2} = 2f^{1/2} |\tilde{h}(f)| , \quad (21)$$

where we have used (17). Both  $\sqrt{S_n(f)}$  and  $\sqrt{S_h(f)}$  have units of  $\text{Hz}^{-1/2}$ . The root PSD is the most frequently plotted quantity in the literature.

The PSD, as defined by (4), has the nice property, demonstrated in (8), that integrated over all positive frequencies it gives the mean square amplitude of the signal in the detector. However, in one important regard it is less appealing than characteristic strain: the height of the source above the detector curve is no longer directly related to the SNR.

#### 2.4. Energy density

A third way of describing the amplitude of a GW is through the energy carried by the waves. This has the advantage of having a clear physical significance. The energy density is most commonly used in sensitivity curves showing stochastic backgrounds of GWs (see section 3.2).

The energy in GWs is described by the Isaacson stress–energy tensor (Misner et al., 1973, section 35.15)

$$T_{\mu\nu} = \frac{c^4}{32\pi G} \langle \partial_\mu \bar{h}_{\alpha\beta} \partial_\nu \bar{h}^{\alpha\beta} \rangle , \quad (22)$$

where the angle brackets denote averaging over several wavelengths or periods, and  $\bar{h}_{\alpha\beta}$  is the transverse-traceless metric perturbation. The energy density  $\rho c^2$  is given by the  $T_{00}$  component of this tensor. Consequently (cf. Berry and Gair, 2013),

$$\rho c^2 = \frac{c^2}{16\pi G} \int_{-\infty}^{\infty} df (2\pi f)^2 \tilde{h}(f) \tilde{h}^*(f) \quad (23)$$

$$= \int_0^{\infty} df \frac{\pi c^2}{4G} f^2 S_h(f) , \quad (24)$$

where the definition (21) have been used. The integrand in Equation (24) is defined as the spectral energy density, the energy per unit volume of space, per unit frequency (Hellings and Downs, 1983)

$$S_E(f) = \frac{\pi c^2}{4G} f^2 S_h(f) ; \quad (25)$$

a corresponding expression for the noise can be formulated by replacing  $S_h(f)$  with  $S_n(f)$ .

Cosmological studies often work in terms of the dimensionless quantity  $\Omega_{\text{GW}}$ , the energy density per logarithmic frequency interval normalised to the critical density of the universe  $\rho_c$ ,

$$\Omega_{\text{GW}}(f) = \frac{f S_E(f)}{\rho_c c^2} . \quad (26)$$

The critical density is

$$\rho_c = \frac{3H_0^2}{8\pi G}, \quad (27)$$

where  $H_0$  is the Hubble constant, commonly parametrized as

$$H_0 = h_{100} \times 100 \text{ km s}^{-1} \text{ Mpc}^{-1}. \quad (28)$$

The reduced Hubble parameter  $h_{100}$  has nothing to do with strain. The most common quantity related to energy density to be plotted on sensitivity curves is  $\Omega_{\text{GW}} h_{100}^2$  (figure A3) as this removes sensitivity to the (historically uncertain) measured value of the Hubble constant.

This quantity has one aesthetic advantage over the others: it automatically accounts for the fact that there is less energy in low frequency waves of the same amplitude. However, unlike characteristic strain, the area between the source and detector curves is no longer simply related to the SNR.

### 2.5. Relating the different descriptions

The dimensionless energy density in GWs  $\Omega_{\text{GW}}$ , spectral energy density  $S_E$ , one-sided PSD,  $S_h$ , characteristic strain  $h_c$  and frequency-domain strain  $\tilde{h}(f)$  are related via

$$H_0^2 \Omega_{\text{GW}}(f) = \frac{8\pi G}{3c^2} f S_E(f) = \frac{2\pi^2}{3} f^3 S_h(f) = \frac{2\pi^2}{3} f^2 [h_c(f)]^2 = \frac{8\pi^2}{3} f^4 |\tilde{h}(f)|^2, \quad (29)$$

using (17), (21), (25), (26) and (27). Corresponding expressions for the noise are obtained by substituting  $S_n(f)$  for  $S_h(f)$ ,  $h_n(f)$  for  $h_c(f)$  and  $\tilde{n}(f)$  for  $\tilde{h}(f)$ .

## 3. Types of source

GW signals can be broadly split into three categories: those from well-modelled sources, for which we have a description of the expected waveform; stochastic backgrounds, for which we can describe the statistical behaviour; and unmodelled (or poorly-modelled) transient sources. The classic example of a well-modelled source is the inspiral of two compact objects, this is discussed in section 3.1. Stochastic backgrounds can either be formed from many overlapping sources, which could be modelled individually, or from some intrinsically random process, these are discussed in section 3.2. An example of an unmodelled (or poorly-modelled) transient source is a supernova; searches for signals of this type are often called burst searches and are discussed in section 3.3.

### 3.1. Inspirals

Inspiralling binaries may be the most important GW source. They spend a variable amount of time in each frequency band. If  $\phi$  is the orbital phase, then the number of cycles generated at frequency  $f$  can be estimated as

$$N_{\text{cycles}} = \frac{f}{2\pi} \frac{d\phi}{df} = \frac{f^2}{\dot{f}}, \quad (30)$$

where an overdot represents the time derivative and  $\dot{\phi} = 2\pi f$ . The squared SNR scales with  $N_{\text{cycles}}$ , so it would be expected that  $h_c(f) \approx \sqrt{N_{\text{cycles}}} |\tilde{h}(f)|$ .

The form for  $h_c$  can be derived from the Fourier transform in the stationary-phase approximation. Consider a source signal with approximately constant (root-mean-square) amplitude  $h_0$  and central frequency  $f'$ . In this case,

$$h(t) = \sqrt{2} h_0 \cos[\phi(t)], \quad (31)$$

$$\tilde{h}(f) = \frac{h_0}{\sqrt{2}} \int_{-\infty}^{\infty} dt \exp \left\{ 2\pi i \left[ \frac{\phi(t)}{2\pi t} - f \right] t \right\} + \exp \left\{ -2\pi i \left[ \frac{\phi(t)}{2\pi t} + f \right] t \right\}. \quad (32)$$

Without loss of generality, we can assume an initial phase of zero, such that  $\phi(0) = 0$ . The largest contribution to the integral comes from where the argument of the exponentials is approximately zero. For the first term, this occurs when  $f = f'$ , then the term in brackets is

$$\left[ \frac{\phi(t)}{2\pi t} - f \right]_{f=f'} = f' + \dot{f}'t + \mathcal{O}(t^2) - f' = \dot{f}'t + \mathcal{O}(t^2). \quad (33)$$

The higher-order terms cause the exponential to oscillate rapidly such that these terms integrate to zero and may be neglected. Performing a similar expansion about  $f = -f'$  for the second term in (32) and then evaluating the Gaussian integrals gives

$$\begin{aligned} \tilde{h}(f) &\simeq \frac{h_0}{\sqrt{2}} \int_{-\infty}^{\infty} dt \exp \left( 2\pi i \dot{f}' t^2 \right) + \exp \left( -2\pi i \dot{f}' t^2 \right) \\ &\simeq \frac{h_0}{\sqrt{2\dot{f}'}}. \end{aligned} \quad (34)$$

From (17) and (34), the characteristic strain for inspiralling sources is given by (Finn and Thorne, 2000)

$$h_c(f) = \sqrt{\frac{2f^2}{\dot{f}}} h_0. \quad (35)$$

Equation (19) should be considered as the definition of characteristic strain and (35) a consequence of it for inspirals. Equation (35) is the relation between  $h_c(f)$  and the instantaneous root-mean-square amplitude  $h_0$  for an inspiralling source; for other types of source a new relation satisfying (19) has to be found.



### 3.2. Stochastic backgrounds

Another important source of GWs is that of stochastic backgrounds, which can be produced from a large population of unresolvable sources. These can be at cosmological distances, where it is necessary to distinguish the frequency in the source rest frame  $f_r$  from the measured frequency  $f$ ; the two are related through the redshift  $z$  via  $f_r = (1 + z)f$ . The comoving number density of sources  $\nu$  producing the background is also a function of redshift; if the sources producing the background are all in the local Universe, then simply set  $\nu(z) = \nu_0\delta(z)$  and replace  $d_L(z)$  with  $d$  in all that follows, where  $d_L(z)$  and  $d$  are respectively the luminosity and comoving distances to the source,  $d_L(z) = (1 + z)d$ .

We shall assume that the individual sources are binaries, in which case the number density of sources is also a function of the component masses. It is convenient to work in terms of the chirp mass, defined as  $\mathcal{M} = \mu^{3/5}M^{2/5}$ , where  $\mu$  is the reduced mass and  $M$  is the total mass of the binary. The comoving number density of sources shall be represented by  $\nu(z, \mathcal{M})$ .

Equation (29) gives an expression for the energy density in GWs per logarithmic frequency interval,

$$f S_E(f) = \frac{\pi c^2}{4G} f^2 [h_c(f)]^2. \quad (36)$$

The total energy emitted in the logarithmic frequency interval  $d(\log f_r)$  by a single binary in the population is  $[dE_{\text{GW}}/d(\log f_r)] d(\log f_r)$ ; the energy density may be written as

$$f S_E(f) = \int_0^\infty dz \frac{d\nu}{dz} \frac{1}{(1+z)} \frac{1}{[d_L(z)]^2} \frac{dE_{\text{GW}}}{d(\log f_r)}, \quad (37)$$

where the factor of  $(1 + z)^{-1}$  accounts for the redshifting of the energy.

For simplicity, consider the background to comprise of binaries in circular orbits, with frequencies  $f_{\text{GW}} = f_r/2$ , which are far from their last stable orbit. The energy radiated may then be calculated using the quadrupole approximation (Peters and Mathews, 1963). The energy in GWs from a single binary per logarithmic frequency interval is

$$\frac{dE_{\text{GW}}}{d(\log f_r)} = \frac{G^{2/3} \pi^{2/3}}{3} \mathcal{M}^{5/3} f_r^{2/3} \quad (38)$$

between an minimum and maximum frequency set by the initial and final radius of the binary orbit. Here, we assume that the maximum and minimum frequencies are outside of the range of our detector and hence can be neglected. Using (36), (37) and (38), an expression for characteristic strain can now be found (Sesana et al., 2008)

$$[h_c(f)]^2 = \frac{4G^{5/3}}{3\pi^{1/3}c^2} f^{-4/3} \int_0^\infty dz \int_0^\infty d\mathcal{M} \frac{d^2\nu}{dz d\mathcal{M}} \frac{1}{[d_L(z)]^2} \left( \frac{\mathcal{M}^5}{1+z} \right)^{1/3}. \quad (39)$$

From (39) it can be seen that the characteristic strain due to a stochastic background of binaries is a power law in frequency with spectral index  $\alpha = -2/3$ . The amplitude of the background depends on the population statistics of the binaries under consideration via  $\nu(z, \mathcal{M})$ . The power law is often parametrised as

$$h_c(f) = A \left( \frac{f}{f_0} \right)^\alpha, \quad (40)$$

and constraints are then placed on  $A$ . In practice, this power law also has upper and lower frequency cut-offs related to the population of source objects. A stochastic background from other sources, such as cosmic strings or relic GWs from the early Universe, can also be written in the same form as (40), but with different spectral indices:  $\alpha = -7/6$  for cosmic strings or  $\alpha$  in the range  $-1$  to  $-0.8$  for relic GWs (Jenet et al., 2006).

An alternative method for graphically representing the sensitivity of a GW detector to stochastic backgrounds, called the *power-law-integrated sensitivity curve*, was suggested by Thrane and Romano (2013). This method accounts for the there being power across all frequencies in the sensitivity band by integrating the noise-weighted signal over frequency. As our aim here is to present stochastic backgrounds alongside other types of sources for comparison, we do not use this approach.

### 3.3. Burst sources

Some sources of GWs can produce signals with large amplitudes, greater than the detector noise. The typical duration of such a signal is short, of the order of a few wave periods, and so there is not time to accumulate SNR in each frequency band as for inspirals. As a consequence, waveform models are not required for detection; we simply rely on identifying the excess power produced by these burst sources. Typically, we may be looking for signals from core-collapse supernovae (Ott, 2009), the late stages of merging compact binaries, or more generally, signals from any unexpected or poorly modelled sources.

Burst searches are often carried out using time–frequency techniques. The data stream from a detector is temporally split into segments, the length of which can be tuned to give greater sensitivity to particular sources. Each segment is then transformed into the frequency domain, whitened and normalised to the noise spectrum of the detector to produce a time–frequency plot. Potential GW signals are identified by searching for clusters of pixels that contain an excess of power (e.g., Abadie et al., 2012a).

The presence of excess power across a number of pixels eliminates modelled noise sources, but such a cluster may also be caused by atypical noise within a detector. We can improve our confidence of a GW signal by making use of information obtained from other GW detectors. Signals across a network of detectors should have compatible arrival times (given the sky direction) as well as consistent amplitudes, frequencies and shapes of the waveform. Different pipelines are currently in use that analyse the signal consistency in different ways:

both coincidence searches (Chatterji et al., 2004) and fully coherent methods (Klimenko et al., 2008) are used.

An important aspect of burst search algorithms is to accurately estimate the noise properties within each time segment. To this extent, null data streams can be constructed that are insensitive to real GW signals. In order to estimate the false alarm rate, the data from different detectors can be shifted in time to remove any genuine coincident GW signals. These time-shifts are then analysed to simulate the potential occurrence of coincident noise events. The algorithms are tuned using time-shifted data to ensure there is no bias in the final search.

As discussed in 3.1, the expected relation between  $h_c(f)$  and a typical waveform  $\tilde{h}(f)$  is

$$h_c(f) = \sqrt{N_{\text{cycles}}} \left| \tilde{h}(f) \right|, \quad (41)$$

where  $N_{\text{cycles}}$  is the number of cycles of radiation generated by the source, which is of order unity for bursts.

An alternative characterisation of the signal amplitude commonly used for burst sources is the root-sum-square of the waveform polarisations:

$$h_{\text{rss}} = \left[ \int dt |h_+(t)|^2 + |h_\times(t)|^2 \right]^{1/2}. \quad (42)$$

For a linearly polarised GW, with  $\tilde{h}(f)$  constant across the bandwidth  $\Delta f$ , this is approximately related to the characteristic strain via

$$h_{\text{rss}} \simeq |\tilde{h}(f)| \sqrt{\Delta f}, \quad (43)$$

where we have neglected the detector response functions (see section 4.1), which are of order unity. In this work, we favour a constant  $h_c(f)$  rather than  $h_{\text{rss}}$  for consistency with the other types of source where the bandwidth is detector specific.

## 4. Detectors

In this section we introduce the detector noise curves used in Appendix A. We begin with a description of the basic operation of detectors. We then discuss ground-based detectors, space-based detectors and PTAs in turn. The latter function somewhat differently than conventional interferometers, so we include a brief introduction to PTA analysis. References for the noise curves used for individual detectors can be found in the relevant subsections, further information about the detectors can be in discovered these. Detectors are frequently upgraded and redesigned, hence, while these curves are believed to be correct at the time of writing, it is best to check for updates from the appropriate science teams before relying on the details given here, although we hope that they shall remain accurate enough for illustrative purposes.

#### 4.1. Operating principle of an interferometric detector

All of the man-made detectors discussed in this section utilise the principle of interferometry. Such detectors work by taking a beam of monochromatic light and splitting it into two beams travelling at some angle to each other. Each beam is passed in to an optical cavity where it undergoes a number of round trips before being recombined to form an interference pattern. The ends of the cavity are, in the ideal case, freely floating test masses which move in response to a passing GW, this effect is measured by observing the changing interference pattern.

The response of a detector to an incident plane-fronted GW depends upon the relative orientations of the detector and the incoming wave. Let us choose the origin of our coordinate system to be the beam-splitter of the interferometer, and  $l_1^i$  and  $l_2^i$  to be unit 3-vectors pointing along the two arms. In the absence of noise the output of the detector is the difference in strain between the two arms (Thorne, 1987)

$$h(t) = \frac{1}{2} h_{ij} (l_1^i l_1^j - l_2^i l_2^j) , \quad (44)$$

where  $h_{ij}$  are the spatial components of the GW metric perturbation. Let  $\hat{r}^i$  be the unit 3-vector pointing towards the source of the GWs, with spherical polar angles  $(\theta, \phi)$  relative to some axes fixed to the detector, and let  $p^i$  and  $q^i$  be unit vectors orthogonal to  $\hat{r}^i$ . We can now define the basis tensors

$$H_{ij}^+ = p_i p_j - q_i q_j , \quad (45)$$

$$H_{ij}^\times = p_i q_j + q_i p_j . \quad (46)$$

There remains a freedom in the coordinates described, a rotation of  $p^i$  and  $q^i$  through an angle  $\psi$  about  $\hat{r}^i$  known as the polarization angle. For a single frequency component, the strain induced by a GW may be written as

$$h_{ij} = A_+ H_{ij}^+ \cos(2\pi f t) + A_\times H_{ij}^\times \cos(2\pi f t + \Delta\phi) , \quad (47)$$

where  $A_+$  and  $A_\times$  are the amplitudes of the two polarisation states. Combining (44) and (47) allows the detector output to be written as

$$h(t) = F^+(\theta, \phi, \psi) A_+ \cos(2\pi f t) + F^\times(\theta, \phi, \psi) A_\times \cos(2\pi f t + \Delta\phi) , \quad (48)$$

where the response functions inherit their angular dependence from the choice of coordinates

$$F^+(\theta, \phi, \psi) = \frac{1}{2} H_{ij}^+ (l_1^i l_1^j - l_2^i l_2^j) , \quad (49)$$

$$F^\times(\theta, \phi, \psi) = \frac{1}{2} H_{ij}^\times (l_1^i l_1^j - l_2^i l_2^j) . \quad (50)$$

The response function of a two-arm interferometric detector is quadrupolar, an example is plotted in figure 1. Throughout this paper detector sensitivity refers to the polarisation



Figure 1: The angular response function of an interferometric detector shown both as a surface plot and in an Aitoff–Hammer projection. The quantity that is plotted is the polarisation average,  $\int d\psi ((F^+)^2 + (F^\times)^2)/2$ . The response is a function of two sky angles,  $\theta$  and  $\phi$ , and varies between 0 and 1. The two detector arms lie in the  $x$ – $y$  plane either side of one of the zeros in the response.

and sky averaged sensitivity  $F$ , where

$$F^2 = \int_0^{2\pi} \frac{d\psi}{2\pi} \int_0^{2\pi} \frac{d\phi}{2\pi} \int_0^\pi \frac{\sin \theta d\theta}{2} \left[ \frac{F^+(\theta, \phi, \psi)^2 + F^\times(\theta, \phi, \psi)^2}{2} \right]. \quad (51)$$

For a single 90°-interferometer, such as LIGO, the sky and polarisation averaged response is  $F = \sqrt{1/5} \approx 0.447$ .

A detector may consist of several interferometers. Let  $F_a$  be the averaged response of the  $a$ -th interferometer, the average response of a network of  $k$  detectors is obtained by adding in quadrature,

$$F_{\text{Total}}^2 = \frac{1}{k} \sum_{a=1}^k F_a^2. \quad (52)$$

The averaging in (51) assumes a uniform distribution of polarisation angles  $\psi$ . This is the case for a stochastic background; however, for a non-inspiralling circular binary, the polarisation is a function of the two spherical polar angles  $(\iota, \xi)$  specifying the orientation of the binary's orbital angular momentum. Here,  $\iota$  is the inclination angle, the polar angle between the orbital angular momentum and the line joining the source to the detector ( $-\hat{r}$ ) and  $\xi$  is the azimuthal angle around the same line. In this case, to characterise the detector sensitivity we average over all four angles  $(\theta, \phi, \iota, \xi)$ . If the binary is inspiralling, then the polarisation depends on still more parameters which need to be averaged over. These more

complicated averages all have the property that they depend on both the detector and the source, hence they are unhelpful for our present purpose separating the source amplitude from the detector sensitivity. Additionally, the different averages do not work out to be so different from each other: Finn and Chernoff (1993) calculated the sensitivity for a detector with the LIGO geometry averaged over the four angles  $(\theta, \phi, \iota, \xi)$  as  $\sqrt{4/25} = 0.4$  times peak sensitivity, which should be compared with the value  $\sqrt{1/5} \approx 0.447$  above. The effect of replacing the true sensitivity with the sky-averaged sensitivity for the LISA detector was considered in detail by Vallisneri and Galley (2012); they also found there is a small difference when considering an entire population of sources. For the remainder of this paper the three-angle average defined in (51) is used.

#### *4.2. Ground-based detectors*

Ground-based detectors are the most numerous. A collection of interferometric detectors are listed in table 1, these are sensitive to GWs in the frequency range  $\mathcal{O}(10\text{--}10^3)$  Hz. They all simulate free-floating test masses by suspending a mass from a pendulum system with natural frequency much greater than that of the GW. Their sensitivity curves include narrow lines that arise from noise sources in the instrument, including resonances in the suspension system and electrical noise at multiples of 60 Hz: these have been removed in the Appendix A figures for clarity. The detectors fall broadly into three categories: first-generation detectors, which have already operated; second-generation detectors currently under construction; and third-generation detectors at the planning stage.

The most notable ground-based detectors are LIGO and Virgo, which work in collaboration, supported by GEO600. LIGO, Virgo and GEO600 have completed science runs as first-generation detectors. As LIGO and Virgo are currently being upgraded their initial configurations are now referred to as Initial LIGO (iLIGO) and Initial Virgo (iVirgo) respectively. The upgraded, second-generation versions are referred to as advanced LIGO (aLIGO) and advanced Virgo (AdV) respectively. LIGO has two observatories: one at Hanford, Washington, which has two detectors; and another at Livingston, Louisiana. There is an agreement to move one of the upgraded Hanford detector systems to a location in India (Iyer et al., 2011; Unnikrishnan, 2013). The GEO600 detector can also operate in a high frequency mode (Willke et al., 2006, GEO-HF). The advanced detectors should start operation in the next couple of years, with LIGO-India following further in the future.

TAMA300 is a Japanese first-generation detector. Its successor, currently under construction, is the Kamioka Gravitational Wave Detector (KAGRA), formerly the Large-scale Cryogenic Gravitational wave Telescope (LCGT), which is located underground in the Kamioka mine. It employs more sophisticated noise-reduction techniques than LIGO or Virgo, such as cryogenic cooling.

The Einstein Telescope (ET) is an ambitious proposal to construct an underground

Table 1: Summary of ground-based laser interferometers.

Detector	Country	Arm length	Approximate date	Generation
GEO600 <sup>a</sup>	Germany	600 m	2001–present	First
TAMA300 <sup>b</sup>	Japan	300 m	1995–present	First
iLIGO <sup>c</sup>	USA	4 km	2004–2010	First
Virgo <sup>d</sup>	Italy	3 km	2007–2010	First
aLIGO <sup>e</sup>	USA	4 km	<i>est.</i> 2015	Second
AdV <sup>f</sup>	Italy	3 km	<i>est.</i> 2016	Second
KAGRA <sup>g</sup>	Japan	3 km	<i>est.</i> 2018	Second
ET <sup>h</sup>	—	10 km	<i>est.</i> 2025	Third

<sup>a</sup>Grote (2010), <sup>b</sup>Ando (2002), <sup>c</sup>Abbott et al. (2009),  
<sup>d</sup>Accadia et al. (2012), <sup>e</sup>Harry (2010), <sup>f</sup>Acernese et al. (2009), <sup>g</sup>Somiya (2012), <sup>h</sup>Hild et al. (2011).

third-generation detector. Its location would provide shielding from seismic noise, allowing it to observe frequencies of 10–10<sup>4</sup> Hz.

We use an interpolation to the data published on <https://wwwcascina.virgo.infn.it/advirgo/> (2013) for the AdV sensitivity curve, an interpolation to the data for version D of the KAGRA detector published on <http://gwcenter.icrr.u-tokyo.ac.jp/en/researcher/parameter> (2013) and analytic fits to the sensitivity curves from Sathyaprakash and Schutz (2009) for the remaining detectors.

#### 4.3. Space-based detectors

Space-based detectors work on similar principles to ground based detectors, but with the test masses residing inside of independent, widely separated satellites. Space-based detectors are sensitive to lower frequency GWs than their ground-based counterparts; this is partly because space based detectors can have much longer arms, and partly because they are unaffected by seismic noise which limits the low frequency performance of ground-based detectors.

The canonical design for a space-based detector is the Laser Interferometer Space Antenna (LISA), which is sensitive to millihertz GWs. LISA would consist of three satellites flying in a triangular constellation with arms of length  $5 \times 10^9$  m in a 1 AU orbit around the Sun, trailing the Earth by 20°. The laser arms in a LISA-like detector are not a cavity, the light only travels once along each arm. eLISA is a rescoped version of LISA designed to probe the same frequency range, while proposals such as the Advanced Laser Interferometer Antenna (ALIA), Big Bang Observer (BBO) and Deci-hertz Interferometer GW Observatory (DECIGO) are designed to probe decihertz GWs.

*4.3.1. LISA and eLISA* The instrumental noise curves for LISA are approximated by the analytic fit given by Sathyaprakash and Schutz (2009), which we use for the plots in Appendix A. When observing individual sources with LISA there is an additional contribution to the noise from a background of unresolvable binaries. This is not included here as we consider the background as a source of GWs (see section 5.2.2). eLISA is a rescoped version of the classic LISA mission, the main differences are shorter arms ( $10^9$  m instead of  $5 \times 10^9$  m), two laser arms instead of three, and a different orbit (drifting away from Earth instead of  $20^\circ$  Earth trailing). The effect of these changes is a slightly reduced peak sensitivity and a shift to higher frequencies. We use an analytic fit to the instrumental noise curve given by Amaro-Seoane et al. (2013).

*4.3.2. DECIGO, ALIA and BBO* These missions are designed to probe the decihertz region of the GW spectrum; they are considerably more ambitious than the LISA or eLISA mission and their launches will be further into the future. We use a simple analytic fit to the sensitivity curve for ALIA (Bender et al., 2013), while for DECIGO and BBO, fits to the sensitivity curves given by Yagi and Seto (2011) are used.

#### *4.4. Pulsar timing arrays*

PTAs can be thought of as naturally occurring interferometers with galactic-scale arm lengths. Accordingly, they are sensitive to much lower frequencies than the detectors previously discussed. Each pulsar is a regular clock and the measured pulse arrival time can be compared against a prediction, leaving a residual which includes the effects of passing GWs. Using an array of these pulsars spread across the sky allows us to correlate residuals between different pulsars, to exploit the fact that GWs influence all pulsars whereas intrinsic pulsar noise does not. The correlation between different pulsars depends only on their angular separation on the sky, and has a distinctive shape, known as the Hellings and Downs curve (Hellings and Downs, 1983).

The redshift of the rate of arrival of pulses for a pulsar at a distance  $L$  from the Solar-System barycentre (SSB), in the direction of the unit spatial vector  $\hat{p}$  induced by a GW travelling in direction of the unit vector  $\hat{\Omega}$  is (Anholm et al., 2009)

$$z(t, \hat{\Omega}) = \frac{1}{2} \frac{\hat{p}^j \hat{p}^i}{1 + \hat{\Omega} \cdot \hat{p}} \left[ h_{ij}^{\text{Pulsar}} \left( t - \frac{L}{c}, \hat{\Omega} \right) - h_{ij}^{\text{Earth}}(t, \hat{\Omega}) \right] = \frac{1}{2} \frac{\hat{p}^j \hat{p}^i}{1 + \hat{\Omega} \cdot \hat{p}} \Delta h_{ij}(t, \hat{\Omega}) . \quad (53)$$

The redshift includes two terms: the pulsar term and the Earth term. The pulsar term is often neglected in PTA analysis as it can be considered as an extra noise term which averages to zero across the array. The experimentally measured quantity is not the redshift but the timing residual, the two are related via

$$R(t, \hat{\Omega}) = \int_0^t dt' z(t', \hat{\Omega}) . \quad (54)$$



All of the pulsars, and the Earth, are subject to the same metric-perturbation field. This may be expressed in terms of its Fourier transform

$$h_{ij}(t, \vec{r}) = \sum_{A=+, \times} \int df \iint_{\mathbb{S}_2} d\hat{\Omega} \tilde{h}_A(f, \hat{\Omega}) e_{ij}^A(\hat{\Omega}) \exp \left[ 2\pi i f \left( t - \frac{\hat{\Omega} \cdot \vec{x}}{c} \right) \right], \quad (55)$$

where  $e_{ij}^A(\hat{\Omega})$  is the  $A$  polarisation basis tensor for direction  $\hat{\Omega}$  and  $\vec{r}$  is the spatial position. Choosing the SSB as the origin of our coordinate system, so the pulsar is at position  $L\hat{p}$ , gives

$$\Delta h_{ij}(t, \hat{\Omega}) = \sum_{A=+, \times} \int df \tilde{h}_A(f, \hat{\Omega}) e_{ij}^A(\hat{\Omega}) \exp(2\pi i f t) \left\{ \exp \left[ -2\pi i f L \left( 1 + \hat{p} \cdot \hat{\Omega} \right) \right] - 1 \right\}. \quad (56)$$

From (53) and (56), the Fourier transform of the redshift  $\tilde{z}(f, \hat{\Omega})$  can be identified as

$$\tilde{z}(f, \hat{\Omega}) = \left\{ \exp \left[ -2\pi i f L \left( 1 + \hat{p} \cdot \hat{\Omega} \right) \right] - 1 \right\} \sum_{A=+, \times} \tilde{h}_A(f, \hat{\Omega}) F^A(\hat{\Omega}), \quad (57)$$

where

$$F^A(\hat{\Omega}) = \frac{e_{ij}^A(\hat{\Omega}) \hat{p}^j \hat{p}^i}{2 \left( 1 + \hat{\Omega} \cdot \hat{p} \right)}. \quad (58)$$

The function  $F^A(\hat{\Omega})$  may be regarded as the PTA equivalent of the detector response functions in (49). The stochastic background of GWs is fully characterised by the one-sided PSD via the expectation value

$$\left\langle \tilde{h}_A^*(f, \hat{\Omega}) \tilde{h}_{A'}(f', \hat{\Omega}') \right\rangle = \frac{1}{2} S_h(f) \delta^{(2)}(\hat{\Omega}, \hat{\Omega}') \delta_{AA'} \delta(f - f'), \quad (59)$$

where  $\delta^{(2)}(\hat{\Omega}, \hat{\Omega}')$  is the delta-function on the sphere. From (57) and (59), the expectation of the product of signals from two different pulsars in directions  $\hat{p}_1$  and  $\hat{p}_2$  may be evaluated as

$$\langle \tilde{z}_1(f) \tilde{z}_2^*(f') \rangle = \frac{1}{2} S_h(f) \delta(f - f') \Gamma(f), \quad (60)$$

where

$$\begin{aligned} \Gamma(f) = & \sum_{A=+, \times} \iint_{\mathbb{S}^2} d\hat{\Omega} \left\{ \exp \left[ 2\pi i f L_1 \left( 1 + \hat{\Omega} \cdot \hat{p}_1 \right) \right] - 1 \right\} \\ & \times \left\{ \exp \left[ -2\pi i f L_2 \left( 1 + \hat{\Omega} \cdot \hat{p}_2 \right) \right] - 1 \right\} F_1^A(\hat{\Omega}) F_2^A(\hat{\Omega}). \end{aligned} \quad (61)$$

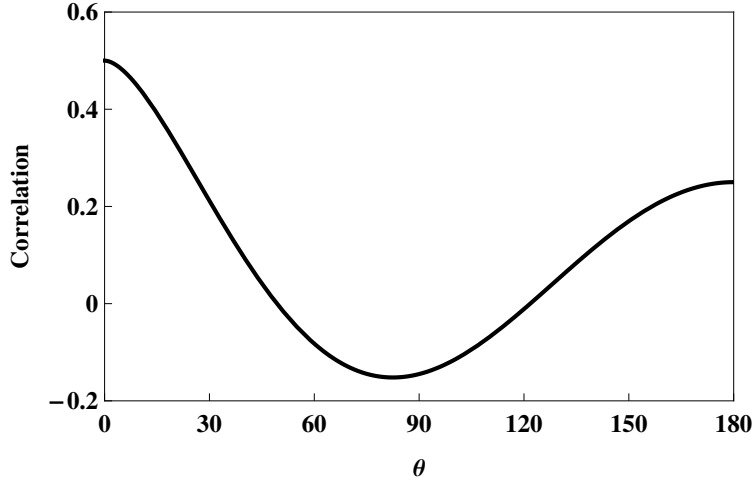


Figure 2: The Hellings and Downs (1983) curve, the correlation between two pulsars separated on the sky by an angle  $\theta$ .

The overlap function  $\Gamma(f)$  tends to a constant value in the limit that the distances to the pulsars are large compared to the wavelength of GWs; PTAs operate in this limit, so the overlap may be approximated as a constant,

$$\Gamma(f) \approx \Gamma_0 = \sum_{A=+, \times} \iint_{\mathbb{S}^2} d\hat{\Omega} F_1^A(\hat{\Omega}) F_2^A(\hat{\Omega}) . \quad (62)$$

Neglecting the exponential terms in the overlap is the frequency-domain equivalent of neglecting the pulsar term in (53). The integral may be evaluated to give an expression depending only on the angle  $\theta$  between the two pulsars; this is the famous Hellings and Downs curve, shown in figure 2,

$$\Gamma_0 = \frac{1}{2} + \frac{3x}{2} \left( \ln x - \frac{1}{6} \right) , \quad (63)$$

where  $x = (1 - \cos \theta)/2$ .

The sensitivity bandwidth of a PTA is set by the sampling properties of the data set. If measurements are spaced in time by  $\delta t$  and taken for a total length of time  $T$ , then the PTA is sensitive to frequencies in the range  $(1/T) < f < (1/\delta t)$ . The characteristic strain that the PTA is sensitive to scales linearly with  $f$  in this range. This gives the wedge-shaped curves plotted in Appendix A. The absolute value of the sensitivity is fixed by normalising to a calculated limit at a given frequency for each PTA. For a discussion of the sensitivities of PTA to both individual sources and stochastic background, see Moore et al. (2014).

There is a discrepancy between the treatment of PTA sensitivity curves here and the higher frequency detectors discussed in sections 4.2 and 4.3. When observing a long-lived

source, such as an inspiral, with a high frequency detector the convention was to define a *characteristic* strain to satisfy (19). Here, the convention is to leave the strain untouched and instead adjust the PTA sensitivity curve with observation time, again to satisfy (19). This discrepancy is an unfortunate result of the conventions in use by the different GW communities; however, it is also natural given the sources under observation. When observing a transient source, such as a burst or inspiral, which changes within the lifetime of the detector, it is natural to consider the detector as performing constantly while the signal changes. However, when observing a monochromatic source or a stochastic background, which is unchanging over the detector lifetime, it is more natural to consider the source as being fixed and the sensitivity of the detector gradually improving. All that is required by the definition in (19) is that the ratio  $h_c(f)/h_n(f)$  is constant.

*4.4.1. Current PTAs* The PTAs currently in operation are the European Pulsar Timing Array (EPTA§; Kramer and Champion, 2013), the Parkes Pulsar Timing Array (PPTA||; Hobbs, 2013) based in Australia, and the North American Nanohertz Observatory for Gravitational waves (NANOGrav¶; McLaughlin, 2013)). There are published limits on the amplitude of the stochastic background from all three detectors: the most recent from EPTA is van Haasteren et al. (2011), from PPTA is Shannon et al. (2013) and from NANOGrav is Demorest et al. (2013). These are all comparable and we use the EPTA limits in Appendix A, the figures show the published limit on  $A$  from equation 40 at a frequency of  $f_0 = 1 \text{ year}^{-1}$ , based on an analysis of five pulsars over approximately ten years.

*4.4.2. The International Pulsar Timing Array* Combining the existing arrays would yield a single PTA using approximately 4 times as many pulsars; this consortium of consortia is known as the International Pulsar Timing Array (IPTA<sup>+</sup>; Manchester and IPTA, 2013). The IPTA curves plotted in the figures are based on 20 pulsars timed for twice as long as the current EPTA.

*4.4.3. SKA* The next great advancement in radio astronomy shall come with the completion of the Square Kilometre Array (SKA; Dewdney et al., 2009). This shall greatly increase the sensitivity of pulsar timing (Kramer et al., 2004). The sensitivity curves plotted in Appendix A for the SKA assume a root-mean-square error on the timing residuals a factor of 10 better than current PTAs, and include 20 pulsars timed for twice as long as the current EPTA.

§ <http://www.epta.eu.org/>

|| <http://www.atnf.csiro.au/research/pulsar/ppta/>

¶ <http://nanograv.org/>

<sup>+</sup> <http://www.ipta4gw.org/>

## 5. Astrophysical sources

All the sources described here are represented by shaded boxes in Appendix A. Sources with short durations (i.e., burst sources) and sources that evolve in time over much longer timescales than our observations are drawn with flat-topped boxes for  $h_c(f)$ . Inspiral binaries, or stochastic backgrounds of binaries, are drawn with a sloping top proportional to  $f^{-2/3}$  for  $h_c(f)$ , which is result derived in section 3.2. The width of the box gives the range of frequencies sources of a given type can have while remaining at a detectable amplitude. The question of the height of the box is more problematic; it would be desirable to normalise each box so that there was a fixed event rate, say one event per year with an amplitude lying within the box. However for many of the sources considered the event rate is subject to a large degree of uncertainty (and estimates change rapidly as our understanding of the astrophysics improves). So instead we take the more definite, but somewhat arbitrary, approach that for each type of source a fiducial event is nominated (with parameters or amplitude detailed in the relevant section below) and the amplitude of this event is used to position the top of the box. The parameters for each fiducial event are chosen such that the resulting amplitude is roughly consistent with the maximum end of current predictions: the boxes indicate where we *could* plausibly find GW sources; the actual event rates could turn out to be substantially lower than this upper bound.

### 5.1. Sources for ground-based detectors

*5.1.1. Neutron star binaries* The inspiral and merger of a pair of neutron stars is the primary target for ground-based detectors. The expected event rate for this type of source is uncertain, but estimates centre around  $\gamma_{\text{NS-NS}} = 1.3 \times 10^{-4} \text{ Mpc}^{-3} \text{ yr}^{-1}$  (Abadie et al., 2012b). Plotted in Appendix A are boxes labelled “*compact binary inspirals*” with amplitudes such that a ratio  $h_c/h_n = 16$  is produced for Advanced LIGO at peak sensitivity and a width between (3–300) Hz, corresponding to expected observable frequencies.

*5.1.2. Supernovae* Simulations of core-collapse supernovae show that GWs between ( $10^2$ – $10^3$ ) Hz can be produced (Kotake et al., 2006). The GW signal undergoes  $\mathcal{O}(1)$  oscillation and is hence burst-like. Dimmelmeyer et al. (2002) calculate the average maximum amplitude of GWs for a supernova at distance  $r$  as

$$h_{\text{max}} = 8.9 \times 10^{-21} \left( \frac{10 \text{ kpc}}{r} \right). \quad (64)$$

The event rate for supernovae is approximately  $\gamma_{\text{SN}} = 5 \times 10^{-4} \text{ Mpc}^{-3} \text{ yr}^{-1}$ . The boxes labelled “*supernova*” plotted in Appendix A correspond to a distance  $r = 300 \text{ kpc}$  with the frequency range quoted above. The LIGO and Virgo detectors have already placed bounds on the event rate for these sources (Abadie et al., 2012a).

*5.1.3. Continuous waves from rotating neutron stars* Rotating neutron stars are a source of continuous GWs if they possess some degree of axial asymmetry (Abbott et al., 2007; Prix, 2009; Aasi et al., 2013). The signals are near monochromatic with a frequency twice the rotation frequency of the neutron star, and are a potential source for ground-based detectors. The amplitude of the GWs depends upon the deformation of the neutron star. The magnitude of the distortion depends upon the neutron star equation of state and the stiffness of the crust, which are currently uncertain (Chamel and Haensel, 2008; Lattimer, 2012); deformations can also be supported by internal magnetic fields (Haskell et al., 2008). Several known pulsars could be sources for the advanced detectors and upper limits from the initial detectors help to constrain the deformations. The boxes labelled “*pulsars*” plotted in Appendix A correspond to the upper limits placed on a GW signal from the Crab pulsar (Aasi et al., 2014b), extrapolated across a frequency range between  $(20\text{--}10^3)$  Hz.

## *5.2. Sources for space-based detectors*

For a review of the GW sources for space-based missions see, for example, Amaro-Seoane et al. (2013), Gair et al. (2013) or Jennrich et al. (2011).

*5.2.1. Massive black hole binaries* Space-based detectors shall be sensitive to equal-mass mergers in the range  $(10^4\text{--}10^7) M_\odot$ . Predictions of the event rate for these mergers range from  $\mathcal{O}(10\text{--}100)$  yr $^{-1}$  for eLISA with SNRs of up to  $10^3$  (Seoane et al., 2013). The large range in the rate reflects our uncertainty in the growth mechanisms of the supermassive black hole population (Volonteri, 2010). Plotted in Appendix A are boxes labelled “ $\approx 10^6$  solar mass binaries” with a ratio  $h_c/h_n = 100$  for eLISA at its peak sensitivity. The range of frequencies plotted is  $(3 \times 10^{-4}\text{--}3 \times 10^{-1})$  Hz; this corresponds to circular binaries in the mass range quoted above.

*5.2.2. Galactic white dwarf binaries* For space-based detectors, these are the most numerous GW sources; they are also the only guaranteed source since several detectable systems (known as verification binaries) have already been identified by electromagnetic observations (Stroeer and Vecchio, 2006).

Galactic binaries divide into two classes: the unresolvable and the resolvable galactic binaries. The unresolvable binaries overlap to form a stochastic background as discussed in section 3.2. The distinction between resolvable and unresolvable is detector specific; here we choose LISA. This boundary will not be too different for eLISA but would move substantially for either of the decihertz detectors. Plotted in Appendix A with the label “*unresolvable galactic binaries*” is the estimate of this background due to Nelemans et al. (2001) where an

observation time of one year has been assumed,

$$h_c(f) = 5 \times 10^{-21} \left( \frac{f}{10^{-3} \text{ Hz}} \right)^{-2/3}. \quad (65)$$

Estimates for the event rate of resolvable binaries centre around  $\mathcal{O}(10^3)$  events for eLISA. The boxes plotted in Appendix A with the label “*resolvable galactic binaries*” have a ratio  $h_c/h_n = 50$  for eLISA at its peak sensitivity. The frequency range of the box is  $(3 \times 10^{-4} - 10^{-2})$  Hz, estimated from Monte Carlo population simulation results presented in Amaro-Seoane et al. (2013).

*5.2.3. Extreme mass-ratio inspirals* EMRIs occur when a compact stellar mass object inspirals into a supermassive black hole. There is extreme uncertainty in the event rate for EMRIs due to the poorly constrained astrophysics in galactic centres (e.g., Merritt et al., 2011); the best guess estimate is around 25 events per year with eLISA with  $\text{SNR} \geq 20$  (Seoane et al., 2013). The boxes labelled “*extreme mass ratio inspirals*” plotted in Appendix A have a characteristic strain of  $h_c = 3 \times 10^{-20}$  at  $10^{-2}$  Hz, which corresponds to a  $10M_\odot$  black hole inspiralling into a  $10^6M_\odot$  black hole at a luminosity distance of 1 Gpc. The frequency width of the box is somewhat unknown; EMRI events can occur into a black hole of any mass, and hence EMRIs can, in principal, occur at any frequency, so the boxes in Appendix A are drawn with a width comparable to that of the LISA sensitivity curve.

### 5.3. Sources for PTAs

*5.3.1. Supermassive black hole binaries* The main target for PTAs is a stochastic background of GWs produced by a population of supermassive black hole binaries at cosmological distances (Sesana et al., 2008). Supermassive black holes are known to lie at the centres of most galaxies and the black hole mergers are associated with the mergers of the host galaxies (Volonteri et al., 2003; Ferrarese and Ford, 2005). The current best 95% confidence limit for the amplitude of the stochastic background is  $h_c = 2.7 \times 10^{-15}$  at a frequency of  $f_0 = 1 \text{ yr}^{-1}$  (Shannon et al., 2013). There is strong theoretical evidence that the actual background lies close to the current limit (Sesana, 2013).

Supermassive black hole binaries at higher frequencies are inspiralling faster and hence there are fewer of them per frequency bin. At a certain frequency, these sources will cease to be a background and become individually resolvable. It is currently unclear whether PTAs will detect an individual binary or a stochastic background first. Plotted in Appendix A with the label “*stochastic background*” is a third of the current limit with a cut off frequency of  $f = 1 \text{ yr}^{-1}$  which is suggested by Monte Carlo population studies (Sesana et al., 2008). For the resolvable sources, labelled “ $\approx 10^9$  solar mass binaries”, the amplitude of the current limit is plotted between  $(3 \times 10^{-9} - 3 \times 10^{-7})$  Hz.

#### 5.4. Cosmological sources

In addition to the sources above, early Universe processes, such as inflation (Grishchuk, 2005) or a first-order phase transition (Binétruy et al., 2012), could have created GWs. More speculatively, it has been hypothesised that cosmic strings could also be a potential source (Damour and Vilenkin, 2005; Binétruy et al., 2012; Aasi et al., 2014*a*). These relic GWs allow us to explore energy scales far beyond those accessible by other means, providing insight into new and exotic physics. The excitement surrounding the tentative discovery by BICEP2 of the imprint of primordial GWs (generated during inflation) in the cosmic microwave background (Ade et al., 2014), and the subsequent flurry of activity, has shown the scientific potential of such cosmological GWs. These GW signals are so alluring because they probe unknown physics; this also makes them difficult to predict. Cosmological stochastic backgrounds have been predicted across a range of frequencies with considerable variation in amplitude. As a consequence of this uncertainty, although we could learn much from measuring these signals, we have not included them amongst the sources in Appendix A.

### 6. Concluding remarks

When quantifying the sensitivity of a GW detector and the loudness of a GW source, there are three commonly used quantities: the characteristic strain, the power spectral density, and the spectral energy density. We have carefully defined these quantities and derived the relationships between them. The characteristic strain (section 2.2) is most directly related to the SNR, the PSD is mostly closely related to the mean square amplitude in the detector, and the energy density has a clear physical interpretation. We have produced example plots using each of these quantities for a wide range of detectors and sources. The predicted source amplitudes are based on astrophysical estimates of the event rates and are subject to varying degrees of uncertainty.\* Interactive versions of these plots, with user-specified detectors and sources, are available on-line at <http://www.ast.cam.ac.uk/~rhc26/sources/>. Trying to summarise an entire field of astronomy on one plot is an impossible task; however, we hope that the figures and analysis presented here provide useful insight.

### Acknowledgments

CJM, RHC and CPLB are supported by the Science & Technology Facilities Council. We are indebted to Jonathan Gair, for useful advice and proof-reading the manuscript. We also thank Stephen Taylor and Justin Ellis for useful conversations about pulsar timing. The authors thanks a number of members of the LIGO–Virgo Scientific Collaboration, especially Chris Messenger, for useful comments and suggestions. This paper has been assigned LIGO

\* There is also the exciting possibility of sources yet to be considered.

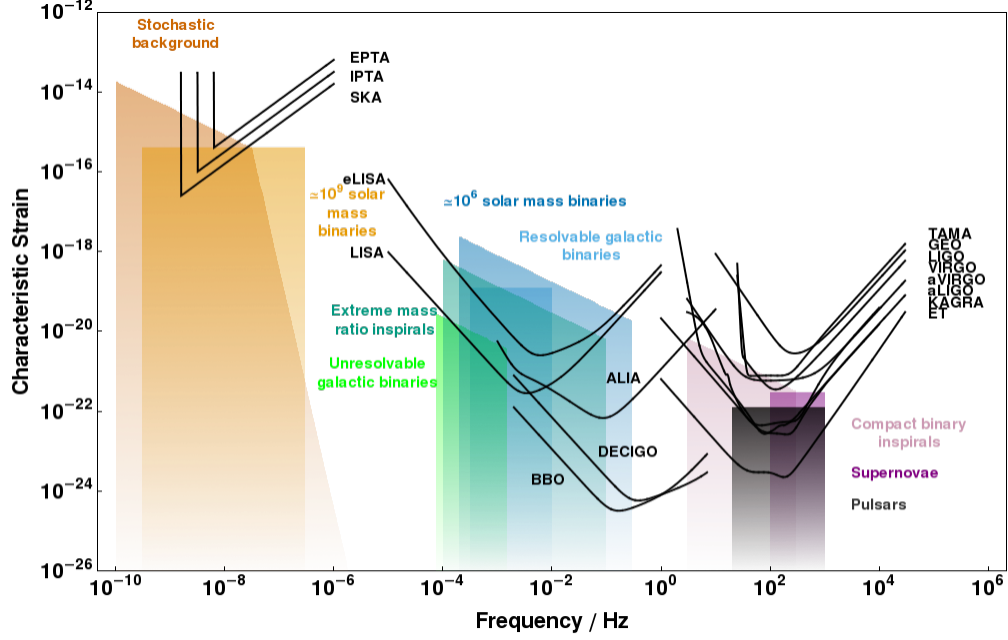


Figure A1: A plot of characteristic strain against frequency for a variety of detectors and sources.

document LIGO-P1400129.

## Appendix A. Sensitivity curves

The plots in this section show all of the detectors and sources described in the main text. Clearer, interactive versions of these plots, allowing for removal of any of the curves, may be created and downloaded on-line, <http://www.ast.cam.ac.uk/~rhc26/sources/>. The detector noise curves all have their resonance spikes removed for clarity.



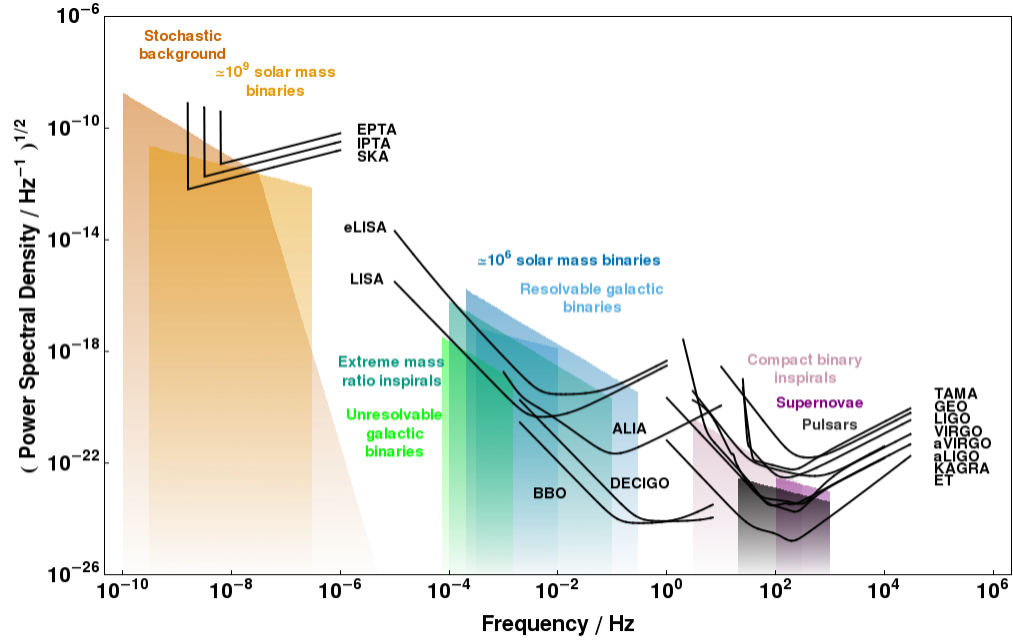


Figure A2: A plot of the square root of power spectral density against frequency for a variety of detectors and sources.

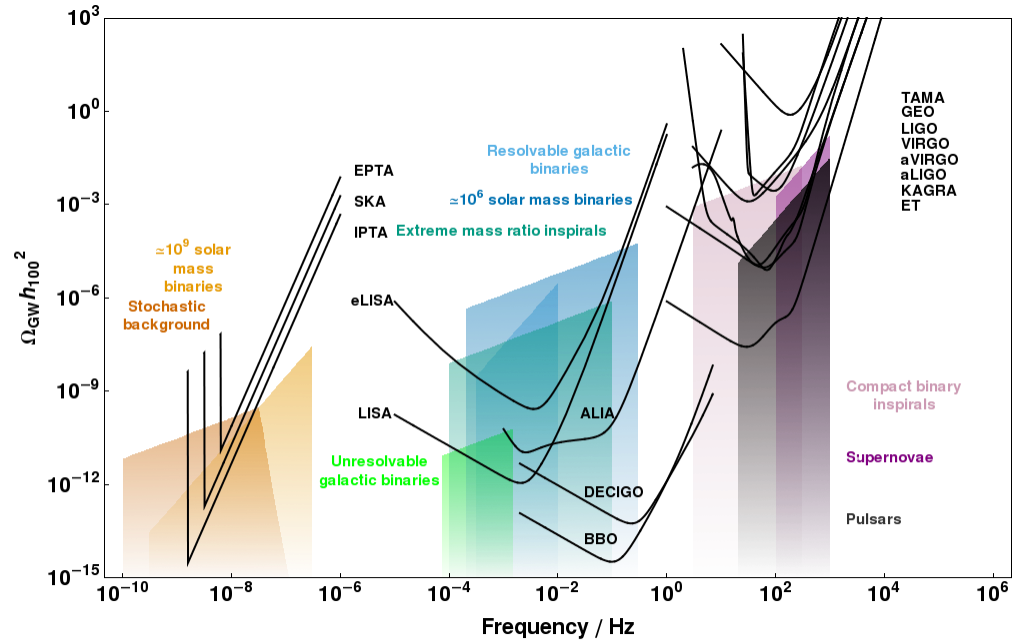


Figure A3: A plot of the dimensionless energy density in GWs against frequency for a variety of detectors and sources.

## References

- Aasi J et al. 2013. Einstein@Home all-sky search for periodic gravitational waves in LIGO S5 data. *Physical Review D* **87**(4), 042001. [arXiv:1207.7176](#).
- Aasi J et al. 2014a. Constraints on Cosmic Strings from the LIGO-Virgo Gravitational-Wave Detectors. *Physical Review Letters* **112**(13), 131101. [arXiv:1310.2384](#).
- Aasi J et al. 2014b. Gravitational waves from known pulsars: results from the initial detector era. *The Astrophysical Journal* **785**(2), 119. [arXiv:1309.4027](#).
- Abadie J et al. 2012a. All-sky search for gravitational-wave bursts in the second joint LIGO-Virgo run. *Physical Review D* **85**(12), 122007. [arXiv:1202.2788](#).
- Abadie J et al. 2012b. Search for gravitational waves from low mass compact binary coalescence in LIGO’s sixth science run and Virgo’s science runs 2 and 3. *Physical Review D* **85**(8), 082002. [arXiv:1111.7314](#).
- Abbott B P et al. 2009. LIGO: the Laser Interferometer Gravitational-Wave Observatory. *Reports on Progress in Physics* **72**(7), 076901. [arXiv:0711.3041](#).
- Abbott B et al. 2007. Searches for periodic gravitational waves from unknown isolated sources and Scorpius X-1: Results from the second LIGO science run. *Physical Review D* **76**(8), 082001. [arXiv:gr-qc/0605028](#).
- Accadia T et al. 2012. Virgo: a laser interferometer to detect gravitational waves. *Journal of Instrumentation* **7**(03), 03012.
- Acernese F et al. 2009 Advanced virgo baseline design Virgo Technical Report VIR-0027A-09. <http://tds.ego-gw.it/itf/tds/file.php?callFile=VIR-0027A-09.pdf>
- Ade P A R et al. 2014. Detection of B-Mode Polarization at Degree Angular Scales by BICEP2. *Physical Review Letters* **112**(24), 241101. [arXiv:1403.3985](#).
- Amaro-Seoane P et al. 2013. eLISA: Astrophysics and cosmology in the millihertz regime. *GW Notes* **6**, 4–110. [arXiv:1201.3621](#).
- Ando M 2002. Current status of TAMA. *Classical and Quantum Gravity* **19**, 1409–1419.
- Anholm M, Ballmer S, Creighton J D E, Price L R and Siemens X 2009. Optimal strategies for gravitational wave stochastic background searches in pulsar timing data. *Physical Review D* **79**(8), 084030. [arXiv:0809.0701](#).
- Bender P L, Begelman M C and Gair J R 2013. Possible LISA follow-on mission scientific objectives. *Classical and Quantum Gravity* **30**(16), 165017.
- Berry C P L and Gair J R 2013. Observing the Galaxy’s massive black hole with gravitational wave bursts. *Monthly Notices of the Royal Astronomical Society* **429**(1), 589–612. [arXiv:1210.2778](#).

- Binétruy P, Bohé A, Caprini C and Dufaux J F 2012. Cosmological backgrounds of gravitational waves and eLISA/NGO: phase transitions, cosmic strings and other sources. *Journal of Cosmology and Astroparticle Physics* **2012**(06), 027. [arXiv:1201.0983](#).
- Chamel N and Haensel P 2008. Physics of Neutron Star Crusts. *Living Reviews in Relativity* **11**(10). [arXiv:0812.3955](#).
- Chatterji S, Blackburn L, Martin G and Katsavounidis E 2004. Multiresolution techniques for the detection of gravitational-wave bursts. *Classical and Quantum Gravity* **21**(20), S1809.
- Cutler C and Flanagan É E 1994. Gravitational waves from merging compact binaries: How accurately can one extract the binary’s parameters from the inspiral waveform? *Physical Review D* **49**(6), 2658–2697. [arXiv:gr-qc/9402014](#).
- Damour T and Vilenkin A 2005. Gravitational radiation from cosmic (super)strings: Bursts, stochastic background, and observational windows. *Physical Review D* **71**(6), 063510. [arXiv:hep-th/0410222](#).
- Demorest P B et al. 2013. Limits on the Stochastic Gravitational Wave Background from the North American Nanohertz Observatory for Gravitational Waves. *ApJ* **762**, 94. [arXiv:1201.6641](#).
- Dewdney P E, Hall P J, Schilizzi R T and Lazio T J L W 2009. The Square Kilometre Array. *Proceedings of the IEEE* **97**(8), 1482–1496.
- Dimmelmeier H, Font J A and Müller E 2002. Relativistic simulations of rotational core collapse II. Collapse dynamics and gravitational radiation. *Astronomy and Astrophysics* **393**, 523–542. [arXiv:astro-ph/0204289](#).
- Ferrarese L and Ford H 2005. Supermassive Black Holes in Galactic Nuclei: Past, Present and Future Research. *Space Science Reviews* **116**(3–4), 523–624. [arXiv:astro-ph/0411247](#).
- Finn L S 1992. Detection, measurement, and gravitational radiation. *Physical Review D* **46**(12), 5236–5249. [arXiv:gr-qc/9209010](#).
- Finn L S and Chernoff D F 1993. Observing binary inspiral in gravitational radiation: One interferometer. *Physical Review D* **47**, 2198–2219. [arXiv:gr-qc/9301003](#).
- Finn L S and Thorne K S 2000. Gravitational waves from a compact star in a circular, inspiral orbit, in the equatorial plane of a massive, spinning black hole, as observed by LISA. *Physical Review D* **62**(12), 124021. [arXiv:gr-qc/0007074](#).
- Foster R S and Backer D C 1990. Constructing a pulsar timing array. *Astrophysical Journal* **361**, 300–308.
- Gair J R, Vallisneri M, Larson S L and Baker J G 2013. Testing General Relativity with Low-Frequency, Space-Based Gravitational-Wave Detectors. *Living Reviews in Relativity* **16**, 7. [arXiv:1212.5575](#).
- Grishchuk L P 2005. Relic gravitational waves and cosmology. *Physics-Uspekhi* **48**(12), 1235–1247. [arXiv:gr-qc/0504018](#).

- Grote H 2010. The GEO 600 status. *Classical and Quantum Gravity* **27**(8), 084003.
- Harry G M 2010. Advanced LIGO: the next generation of gravitational wave detectors. *Classical and Quantum Gravity* **27**(8), 084006.
- Haskell B, Samuelsson L, Glampedakis K and Andersson N 2008. Modelling magnetically deformed neutron stars. *Monthly Notices of the Royal Astronomical Society* **385**(1), 531–542. [arXiv:0705.1780](#).
- Hellings R W and Downs G S 1983. Upper limits on the isotropic gravitational radiation background from pulsar timing analysis. *Astrophysical Journal Letters* **265**, L39–L42.
- Hild S et al. 2011. Sensitivity studies for third-generation gravitational wave observatories. *Classical and Quantum Gravity* **28**(9), 094013. [arXiv:1012.0908](#).
- Hobbs G 2013. The Parkes Pulsar Timing Array. *Classical and Quantum Gravity* **30**(22), 224007. [arXiv:1307.2629](#).
- Iyer B et al. 2011 LIGO-India, Proposal of the Consortium for Indian Initiative in Gravitational-wave Observations (IndIGO) Technical Report M1100296. <https://dcc.ligo.org/cgi-bin/DocDB/ShowDocument?docid=75988>
- Jenet F A et al. 2006. Upper Bounds on the Low-Frequency Stochastic Gravitational Wave Background from Pulsar Timing Observations: Current Limits and Future Prospects. *Astrophysical Journal* **653**, 1571–1576. [arXiv:astro-ph/0609013](#).
- Jennrich O et al. 2011 NGO Revealing a hidden Universe: opening a new chapter of discovery Technical Report ESA/SRE(2011)19 European Space Agency Noordwijk.
- Klimenko S, Yakushin I, Mercer A and Mitselmakher G 2008. A coherent method for detection of gravitational wave bursts. *Classical and Quantum Gravity* **25**(11), 114029.
- Kotake K, Sato K and Takahashi K 2006. Explosion mechanism, neutrino burst and gravitational wave in core-collapse supernovae. *Reports on Progress in Physics* **69**(4), 971–1143. [arXiv:astro-ph/0509456](#).
- Kramer M and Champion D J 2013. The European Pulsar Timing Array and the Large European Array for Pulsars. *Classical and Quantum Gravity* **30**(22), 224009.
- Kramer M et al. 2004. Strong-field tests of gravity using pulsars and black holes. *New Astronomy Reviews* **48**(11–12), 993–1002. [arXiv:astro-ph/0409379](#).
- Lattimer J M 2012. The Nuclear Equation of State and Neutron Star Masses. *Annual Review of Nuclear and Particle Science* **62**(1), 485–515. [arXiv:1305.3510](#).
- Manchester R N and IPTA 2013. The International Pulsar Timing Array. *Classical and Quantum Gravity* **30**(22), 224010.
- McLaughlin M A 2013. The North American Nanohertz Observatory for Gravitational Waves. *Classical and Quantum Gravity* **30**(22), 224008. [arXiv:1310.0758](#).
- Merritt D, Alexander T, Mikkola S and Will C M 2011. Stellar dynamics of extreme-mass-ratio inspirals. *Physical Review D* **84**(4), 044024. [arXiv:1102.3180](#).

- Misner C W, Thorne K S and Wheeler J A 1973 *Gravitation* W.H. Freeman and Co. San Fansisco.
- Moore C J, Taylor S R and Gair J R 2014. Estimating the sensitivity of pulsar timing arrays. [arXiv:1406.5199](#).
- Nelemans G, Yungelson L R and Portegies Zwart S F 2001. The gravitational wave signal from the Galactic disk population of binaries containing two compact objects. *Astronomy and Astrophysics* **375**, 890–898. [arXiv:astro-ph/0105221](#).
- Ott C D 2009. The gravitational-wave signature of core-collapse supernovae. *Classical and Quantum Gravity* **26**(6), 063001.
- Peters P C and Mathews J 1963. Gravitational Radiation from Point Masses in a Keplerian Orbit. *Physical Review* **131**, 435–440.
- Prix R 2009 in W Becker, ed., ‘Neutron Stars and Pulsars’ Astrophysics and Space Science Library Springer Berlin chapter 24, pp. 651–685.
- Sathyaprakash B S and Schutz B F 2009. Physics, Astrophysics and Cosmology with Gravitational Waves. *Living Reviews in Relativity* **12**, 2. [arXiv:0903.0338](#).
- Seoane P A et al. 2013. The Gravitational Universe. [arXiv:1305.5720](#).
- Sesana A 2013. Systematic investigation of the expected gravitational wave signal from supermassive black hole binaries in the pulsar timing band. *Monthly Notices of the Royal Astronomical Society* **433**, L1–L5. [arXiv:1211.5375](#).
- Sesana A, Vecchio A and Colacino C N 2008. The stochastic gravitational-wave background from massive black hole binary systems: implications for observations with Pulsar Timing Arrays. *Monthly Notices of the Royal Astronomical Society* **390**, 192–209. [arXiv:0804.4476](#).
- Shannon R M et al. 2013. Gravitational-wave limits from pulsar timing constrain supermassive black hole evolution. *Science* **342**(6156), 334–337. [arXiv:1310.4569](#).
- Somiya K 2012. Detector configuration of KAGRA-the Japanese cryogenic gravitational-wave detector. *Classical and Quantum Gravity* **29**(12), 124007. [arXiv:1111.7185](#).
- Stroeer A and Vecchio A 2006. The LISA verification binaries. *Classical and Quantum Gravity* **23**, 809. [arXiv:astro-ph/0605227](#).
- Thorne K S 1987 in S. W Hawking and W Israel, eds, ‘Three Hundred Years of Gravitation’ Cambridge University Press Cambridge chapter 9, pp. 330–458.
- Thrane E and Romano J D 2013. Sensitivity curves for searches for gravitational-wave backgrounds. *Physical Review D* **88**(12), 124032. [arXiv:1310.5300](#).
- Unnikrishnan C S 2013. IndIGO and Ligo-India Scope and Plans for Gravitational Wave Research and Precision Metrology in India. *International Journal of Modern Physics D* **22**(1), 1341010.

- Vallisneri M and Galley C R 2012. Non-sky-averaged sensitivity curves for space-based gravitational-wave observatories. *Classical and Quantum Gravity* **29**(12), 124015. [arXiv:1201.3684](#).
- van Haasteren R et al. 2011. Placing limits on the stochastic gravitational-wave background using European Pulsar Timing Array data. *Monthly Notices of the Royal Astronomical Society* **414**(4), 3117–3128. [arXiv:1103.0576](#).
- Volonteri M 2010. Formation of supermassive black holes. *The Astronomy and Astrophysics Review* **18**(3), 279–315. [arXiv:1003.4404](#).
- Volonteri M, Haardt F and Madau P 2003. The Assembly and Merging History of Supermassive Black Holes in Hierarchical Models of Galaxy Formation. *The Astrophysical Journal* **582**(2), 559–573. [arXiv:astro-ph/0207276](#).
- Wiener N 1949 *The extrapolation, interpolation and smoothing of stationary time series* The M.I.T. Press Cambridge, Massachusetts.
- Willke B et al. 2006. The GEO-HF project. *Classical and Quantum Gravity* **23**, 207.
- Yagi K and Seto N 2011. Detector configuration of DECIGO/BBO and identification of cosmological neutron-star binaries. *Physical Review D* **83**(4), 044011. [arXiv:1101.3940](#).